RSC Advances

PAPER

View Article Online
View Journal | View Issue

Cite this: *RSC Adv.*, 2025, **15**, 22682

SCN–IgG functionalized $NaYF_4$:Yb^{3+}/(Er^{3+},Tm^{3+}) upconversion nanoparticles for targeted fluorescence imaging of liver cancer cells

Ha Thi Phuong,[a] Tran Thu Huong,*[b] Le Thi Vinh,*[c] Do Thi Thao,[d] Le Anh Tu,[b] Tong Quang Cong,[b] Nguyen Duc Van[b] and Tran Quoc Tien[b]

Received 2nd June 2025
Accepted 20th June 2025

DOI: 10.1039/d5ra03912f

rsc.li/rsc-advances

Lanthanide-doped upconversion nanoparticles (UCNPs) offer significant potential for bioimaging due to their ability to convert near-infrared (NIR) excitation into visible emission. In this study, $NaYF_4$:Yb^{3+}/(Er^{3+},Tm^{3+}) UCNPs were synthesized *via* a hydrothermal method and sequentially functionalized with a silica shell, amine, thiocyanate (SCN), and immunoglobulin G (IgG) to enhance their biocompatibility and targeting capabilities. Structural characterization confirmed the formation of highly crystalline β-$NaYF_4$ cores with uniform morphology and successful surface modification. The functionalized nanoparticles exhibited strong upconversion luminescence under 980 nm excitation, with multicolor emission dominated by red light (~660 nm). Fluorescence microscopy and flow cytometry demonstrated selective labeling of HepG2 liver cancer cells, achieving a labeling efficiency of 18.10% for SCN–IgG-conjugated nanoparticles—significantly higher than in unmodified controls. These findings demonstrate that SCN–IgG-functionalized UCNPs are effective and selective nanoprobes for targeted fluorescence imaging and hold promise for the early diagnosis of liver cancer.

1. Introduction

Hepatocellular carcinoma (HCC) is one of the most prevalent and lethal forms of liver cancer, often diagnosed at advanced stages due to the lack of sensitive early detection methods. In recent years, nanotechnology-based diagnostic platforms have shown great promise in improving cancer detection, particularly through the development of fluorescent nanoprobes for targeted imaging.[1–4] Various applications of upconversion nanomaterials systems have been explored, *e.g.*, triplet–triplet annihilation (TTA) for energy conversion, $NaYF_4$:Yb^{3+},Er^{3+} UCNPs for bioimaging and photodynamic therapy (PDT), as well as rare-earth-modified inorganic semiconductor photocatalysts for efficient solar energy conversion. Additionally, plasmon-enhanced UCNPs with tunable emission properties have also been reported.[5–8] Among these, lanthanide-doped upconversion nanoparticles (UCNPs) have attracted significant interest due to their unique ability to convert near-infrared (NIR) light into visible emission *via* multiphoton excitation. This upconversion luminescence (UCL) provides several key advantages, including deep tissue penetration, low background autofluorescence, and minimal photodamage, making UCNPs highly suitable for biological imaging applications.[9–14]

$NaYF_4$ has been widely recognized as the most efficient host lattice for upconversion processes due to its low phonon energy and high luminescence efficiency. In particular, $NaYF_4$:Yb^{3+}/Er^{3+} systems have been extensively studied for their strong green (~540 nm) and red (~650 nm) emissions under 980 nm excitation.[15,16] However, to broaden the emission spectrum and enhance optical output, co-doping strategies involving both Er^{3+} and Tm^{3+} ions have been adopted. Co-doping with ytterbium (Yb^{3+}), erbium (Er^{3+}), and thulium (Tm^{3+}) enables multicolor emission—blue (~475 nm), green (~545 nm), and red (~660 nm)—under a single NIR excitation source, thereby facilitating multiplexed imaging and improving detection sensitivity.

Despite their promising optical properties, the biomedical application of UCNPs remains limited by challenges related to surface modification and biofunctionalization. These include the need for colloidal stability, biocompatibility, and selective cell-targeting capability.[17–19] To overcome these limitations, various surface engineering strategies have been explored. Among them, silica encapsulation has proven particularly effective in providing a chemically robust and optically transparent shell that preserves luminescence while offering functional groups for subsequent modification.[20–25]

In particular, 3-thiocyanatopropyltriethoxysilane (SCN–PTES) offers a direct route to introduce thiocyanate (–SCN)

[a]*Department of Chemistry, Hanoi Medical University, 1 Ton That Tung, Hanoi 100000, Vietnam*

[b]*Institute of Materials Science, Vietnam Academy of Science and Technology, 18 Hoang Quoc Viet, Hanoi 100000, Vietnam. E-mail: huongtt.ims@gmail.com*

[c]*Faculty of Basic Science, Hanoi University of Mining and Geology, 18 Pho Vien, Hanoi 100000, Vietnam. E-mail: levinhmdc@gmail.com*

[d]*Institute of Biology, Vietnam Academy of Science and Technology, 18 Hoang Quoc Viet, Hanoi 100000, Vietnam*

groups, which can form covalent thiourea linkages with primary amines in biomolecules such as antibodies. This approach enables stable and site-specific conjugation without disrupting the optical properties of the UCNPs.[26–31]

In this study, we report the synthesis of $NaYF_4$:Yb^{3+}/(Er^{3+},Tm^{3+}) UCNPs, their surface modification with a silica shell and SCN groups, and subsequent conjugation with immunoglobulin G (IgG) for targeted bioimaging of HepG2 liver cancer cells. Structural and spectroscopic analyses confirmed successful functionalization without compromising crystal phase or luminescence intensity. Most importantly, fluorescence microscopy and flow cytometry demonstrated that the SCN–IgG-conjugated UCNPs enabled highly selective labeling of HepG2 cells, with significantly higher efficiency than non-functionalized controls. These findings support the potential of SCN-based biofunctionalization as a robust strategy for developing selective and efficient upconversion nanoprobes for cancer diagnostics.

2. Materials and methods

2.1. Materials

All chemicals were of analytical grade and used without further purification. Yttrium(III) nitrate hexahydrate $Y(NO_3)_3 \cdot 6H_2O$, (99.9%), ytterbium(III) nitrate pentahydrate $Yb(NO_3)_3 \cdot 5H_2O$, (99.9%), erbium(III) nitrate pentahydrate $Er(NO_3)_3 \cdot 5H_2O$ (99.9%), thulium(III) nitrate pentahydrate $Tm(NO_3)_3 \cdot 5H_2O$ (99.9%), tetraethyl orthosilicate (TEOS (99.9%)), sodium fluoride NaF (99%), ammonium hydroxide (NH_4OH (25%)), 3-triethoxysilylpropyl amine APTES (98%), and 3-triethoxysilylpropyl thiocyanate SCNPTES (95%) were purchased from Sigma-Aldrich. Trisodiumcitrate dihydrate $HOC(COONa)(CH_2COONa)_2 \cdot 2H_2O$ (99%), sodium hydroxide NaOH (99%) were provided from Merck. Ethanol C_2H_5OH (99.8%) and oleic acid $CH_3(CH_2)_7CH{=}CH(CH_2)_7COOH$ (92%) were supplied by Fisher Scientific. HepG2 cells were a kind gift from Prof. Chi-Ying F. Huang, National Yang Ming Chiao Tung, Taipei, Taiwan.

2.2. Synthesis of $NaYF_4$:Yb^{3+}/(Er^{3+}, Tm^{3+}) nanoparticles

The upconversion nanoparticles were synthesized using a hydrothermal method. Rare-earth precursors were mixed in a molar ratio of $Y^{3+}:Yb^{3+}:Er^{3+}:Tm^{3+} = 78:20:1:1$. The mixture was combined with NaF, NaOH, and oleic acid in an ethanol–water solution, then vigorously stirred and transferred to a Teflon-lined stainless-steel autoclave. The autoclave was sealed and heated at 200 °C for 24 hours. The resulting product was collected by centrifugation, washed thoroughly with ethanol and deionized water, and dried at 70 °C.

2.3. Silica coating and surface functionalization

The obtained nanoparticles were dispersed in ethanol and coated with a silica shell *via* the Stöber method, involving hydrolysis of TEOS in the presence of NH_4OH. Subsequently, the silica-coated nanoparticles were functionalized with amine groups ($-NH_2$) by reacting with APTES for 24 hours. For thiocyanate functionalization, SCN–PTES was added to the amine-modified nanoparticles and stirred in phosphate-buffered saline (PBS, 0.5 M, pH 5) at a concentration of 5 g L^{-1} for 30 minutes. The SCN-modified nanoparticles were then incubated with varying concentrations of IgG in the presence of glycerol at room temperature for 6 hours. Finally, the biofunctionalized nanoparticles were centrifuged at 5900 rpm, washed three times with water, and stored at 4 °C in sealed containers.

2.4. Liver cancer cell culture, fluorescence imaging of cells

In this study, the experiments were implemented on HepG2 liver cancer cells which were maintained in Dulbecco's Modified Eagle Medium (DMEM – Invitrogen) with fetal bovine serum (10%) (Sigma) and gentamicin (50 μg mL^{-1}) at 37 °C and 5% CO_2 in a humidified atmosphere. To study the uptake capacity of the functionalized $NaYF_4$:Yb^{3+}/(Er^{3+},Tm^{3+})@silica–NH–SCN–IgG, the liver cancer cells (10^4 cells per ml) at log phase were seeded in 24 well plates, then incubated for 24 hours. Polyethylene glycol 1500 (Sigma) and UCNP samples $NaYF_4$:Yb^{3+}/(Er^{3+},Tm^{3+}), $NaYF_4$:Yb^{3+}/(Er^{3+},Tm^{3+})@silica–NH–SCN–IgG were added to the wells at a final concentration of 2% and incubated for 3 hours. After the assigned time, the cultured medium was discarded. The cells were then washed with phosphate buffer saline (PBS pH 7.4) three times before fixed with formaldehyde 10% in 30 min at room temperature. The fixed cells were then formaldehyde discarded, PBS washed three times before staining with Hoechst 33 342 solution (2 μg mL^{-1}) for 15 minutes at room temperature. After staining, the solution was removed, and the cells were washed with PBS three times again. The cell images were obtained using the fluorescence-inverted microscope ZEISS AXIOSCOPE A1 with 200× magnification.

2.5. Cellular uptake analysis using flowcytometry

The HepG2 cells were cultured in the DMEM supplemented with L-glutamine, sodium pyruvat, $NaHCO_3$, penicillin/streptomycin, 10% FBS (Fetal Bovine Serum). Cells at the density of 1×10^4 cells per mL were pre-cultured in 6-well plate at 37 °C, 5% CO_2 in the incubator for 24 hours. Then, the medium was replaced with DMEM (w/o FBS) added 2% of either $NaYF_4$:Yb^{3+}/(Er^{3+},Tm^{3+}) or $NaYF_4$:Yb^{3+}/(Er^{3+},Tm^{3+})@silica–NH–SCN–IgG and incubated for 3 hours at 37 °C, 5% CO_2 incubator. Then, the cells were detached with 0.05% trypsin–EDTA, centrifuged at 1000 rpm for 5 minutes to obtain the cell pellets. The pellets were washed with cold PBS twice before resuspending in PBS 1× for analyzing with flowcytometry Novocyte system (ACEA Bioscience inc.) and NovoExpress software. The cells were requested for light protection.

2.6. Characterization techniques

Structural and morphological characterizations were performed using X-ray diffraction (XRD; D8 Advance, Bruker, Germany) and field-emission scanning electron microscopy (FESEM; S-4800, Hitachi, Japan).

Surface functionalization was confirmed by Fourier-transform infrared spectroscopy (FTIR; Spectrum Two, PerkinElmer, USA). FTIR spectra were recorded in the transmittance

mode over the range of 4000–400 cm^{-1}. For FTIR analysis, the powdered nanoparticle samples were thoroughly dried and then finely ground with potassium bromide (KBr) at a ratio of approximately 1 : 100 (sample : KBr, w/w). The mixture was pressed into thin pellets using a hydraulic press.

The upconversion luminescence properties were analyzed using a photoluminescence measurement system (iHR320, Horiba) under 980 nm continuous-wave (CW) laser excitation (estimated optical power density in the range of several tens of W cm^{-2}). Measurements were conducted on dry powder samples, with equal amounts of each sample gently pressed into standard sample holders featuring a 1 mm diameter well. All measurement parameters—including excitation power, acquisition time, and optical configuration—were kept constant across samples to ensure reliable intensity comparison. To minimize light scattering due to particle aggregation, the samples were thoroughly dried, finely ground, and uniformly dispersed prior to measurement.

In vitro bioimaging experiments were performed using HepG2 liver cancer cells incubated with either bare $NaYF_4$:Yb^{3+}/(Er^{3+},Tm^{3+}) nanoparticles or functionalized $NaYF_4$:Yb^{3+}/(Er^{3+},Tm^{3+})@silica–NH–SCN–IgG nanoparticles. Fluorescence microscopy was then employed to evaluate their targeting performance.

3. Results and discussion

3.1. Morphological characterization

The morphology of the synthesized $NaYF_4$:Yb^{3+}/(Er^{3+},Tm^{3+}) nanoparticles was examined using field-emission scanning electron microscopy (FESEM), as shown in Fig. 1.

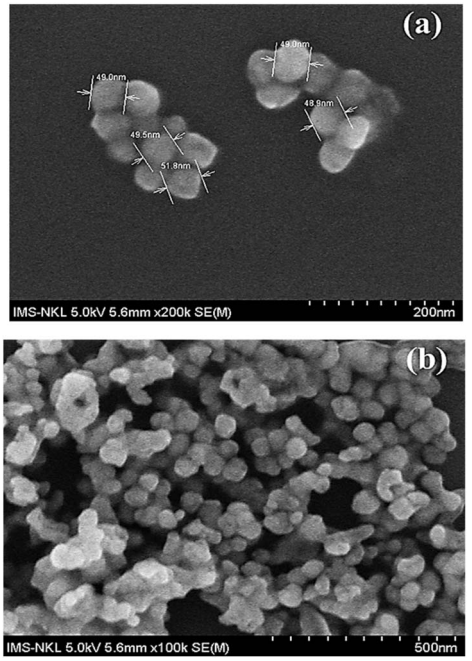

Fig. 1 FESEM images of $NaYF_4$:Yb^{3+}/(Er^{3+},Tm^{3+}) nanoparticles: (a) high-magnification image at 200 nm scale and (b) lower magnification image at 500 nm scale, respectively.

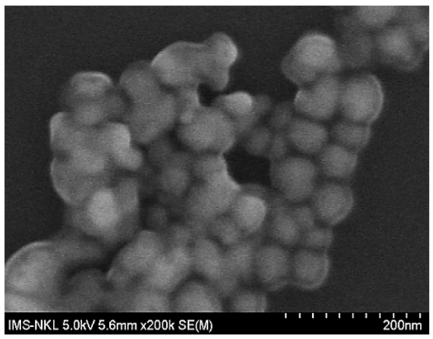

Fig. 2 FESEM images of $NaYF_4$:Yb^{3+}/(Er^{3+},Tm^{3+})@silica–NH–SCN–IgG nanoparticles at 200 nm scale.

The high-resolution image (Fig. 1a) reveals that the particles exhibit well-defined morphology with near-spherical. The measured particle diameters fall within the desired range of 45–55 nm. The lower-magnification view (Fig. 1b) further confirms that the sample is well-dispersed with minimal aggregation, indicating efficient synthesis during the hydrothermal process.

After surface modification with silica, amine, thiocyanate, and subsequent IgG conjugation, the morphology of the nanoparticles was re-examined by FESEM (Fig. 2). The $NaYF_4$:Yb^{3+}/(Er^{3+},Tm^{3+})@silica–NH–SCN–IgG particles retain their overall shape and uniformity, with a slight increase in diameter (~50–60 nm) compared to the unmodified sample. The increase in particle size and slightly rougher surface texture are consistent with the formation of an amorphous silica shell and subsequent bioconjugation – thiocyanate groups with IgG molecules. This change in morphology supports the successful formation of the silica layer and further functionalization, which is essential for subsequent bioconjugation with targeting ligands or antibodies. These results confirm that the nanoparticles retain their structural integrity after surface modification and are morphologically suitable for biomedical applications, including cellular.

3.2. Structure characterization

The crystalline phase of the synthesized nanoparticles were evaluated by X-ray diffraction (XRD), and the results are shown in Fig. 3. The diffraction peaks of the uncoated sample $NaYF_4$:Yb^{3+}/(Er^{3+},Tm^{3+}) (red line-(1)) match well with the standard hexagonal β-$NaYF_4$ phase (JCPDS no. 28-1192), indicating the successful formation of the desired crystal structure.

Characteristic peaks at 2θ values of approximately ~28.2, 30.0, 32.7, 34.8, 40.0, 43.5, 47.0, 52.7, 55.5, 58.3, 60.3, 62.9° correspond to the (1 0 0), (1 0 1), (1 0 2), (1 1 0), (1 0 3), (2 0 0), (1 1 2), (2 0 1), (1 0 4), (2 0 2), (2 1 0) lattice planes of β-$NaYF_4$, respectively. The narrow and intense diffraction peaks suggest high crystallinity of the as-prepared nanomaterials. After silica coating and amine, thiocyanate functionalization with IgG-conjugated (blue line – (2)), the diffraction pattern remains largely unchanged, retaining all the key peaks associated with the β-$NaYF_4$ phase. This indicates that the silica, amine, thiocyanate groups promoted the covalent IgG conjugation shell is

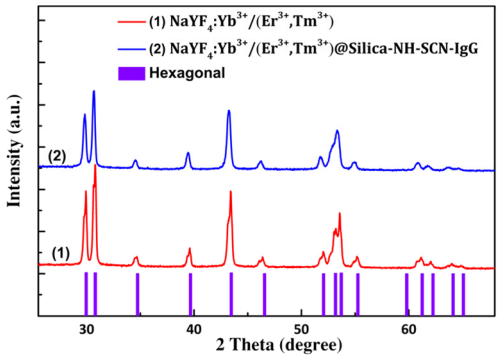

Fig. 3 X-ray diffraction patterns of the (1) $NaYF_4$:Yb^{3+}/(Er^{3+}, Tm^{3+}) and (2) $NaYF_4$:Yb^{3+}/(Er^{3+}, Tm^{3+})@silica–NH–SCN–IgG nanoparticles.

amorphous and does not interfere with the crystal structure of the core material.

The diffraction intensity slightly decreases without peak broadening or shifting, suggesting that the shell did not alter the crystal structure of the core material. No additional peaks are observed, confirming the phase purity of the coated nanoparticles.

To estimate the average crystallite size, the Scherrer equation was applied to the most intense diffraction peak located at approximately $2\theta \approx 30.0°$:

$$D = \frac{K \cdot \lambda}{\beta \cdot \cos\theta}$$

where D is the crystallite size (nm), K is the shape factor (taken as 0.9), λ is the X-ray wavelength (0.154 nm, Cu Kα), β is the full width at half maximum (FWHM) in radians, and θ is the Bragg angle. With an FWHM of 0.17°, the calculated average crystallite size was approximately 48.3 nm.

This crystallite size is in good agreement with the particle size range of 45–60 nm observed in FESEM images, suggesting that the nanoparticles are largely monocrystalline. The consistency between XRD and FESEM results indicates that almost each nanoparticle corresponds to a single crystal domain with minimal aggregation or polycrystallinity.

Fourier-transform infrared (FTIR) spectroscopy was used to confirm the surface modification and functional group incorporation on the synthesized nanoparticles. Fig. 4 displays the FTIR spectra of $NaYF_4$:Yb^{3+}/(Er^{3+},Tm^{3+}) nanoparticles before (sample 1) and after surface modification with silica, amine, thiocyanate (SCN), and immunoglobulin G (IgG) (sample 2).

Both samples exhibit a broad absorption band in the range of 3350–3450 cm^{-1}, which is attributed to the O–H stretching vibrations of adsorbed water or surface hydroxyl groups. The absorption band at approximately 2930 cm^{-1} corresponds to the asymmetric and symmetric stretching vibrations of C–H bonds, likely originating from residual organic surfactants such as oleic acid used during synthesis. In sample 2, a distinct absorption band at ~1660 cm^{-1} corresponds to N–H bending vibrations from amine groups (introduced *via* APTES) and/or C=O stretching from IgG molecules, indicating successful protein conjugation. A weak but distinct peak at ~2050 cm^{-1} is exclusively observed in sample 2 and corresponds to the C≡N stretching vibration, which is characteristic of thiocyanate (–SCN) groups. Despite its low intensity, this band provides compelling evidence of successful SCN incorporation *via* amine linkers onto the silica surface.[32–34]

Notably, strong absorption bands observed between 1000 and 1150 cm^{-1} in sample 2 are characteristic of Si–O–Si stretching vibrations, confirming the presence of a silica shell. In the low wavenumber region below 1000 cm^{-1}, both spectra exhibit absorption bands associated with lanthanide–fluoride (Ln–F) vibrations, particularly around 460–690 cm^{-1}, validating the $NaYF_4$:Yb^{3+}/(Er^{3+},Tm^{3+}) core structure.[35,36]

In summary, the FTIR results clearly confirm the stepwise surface modification process—including silica coating, amination, SCN functionalization, and IgG conjugation—which is crucial for enhancing colloidal stability, biocompatibility, and targeted bioimaging performance of the upconversion nanoparticles.

3.3. Luminescence properties

Fig. 5 presents the upconversion photoluminescence (UCPL) spectra of $NaYF_4$:Yb^{3+}/(Er^{3+},Tm^{3+}) nanoparticles before and after surface modification.

Under 980 nm excitation, at ~475 nm (blue) corresponds to the $^1G_4 \rightarrow {}^3H_6$ transition of Tm^{3+}, ~410 nm band: corresponds to $^2G_{9/2} \rightarrow {}^4I_{15/2}$ transition, at ~520–560 nm band (green):

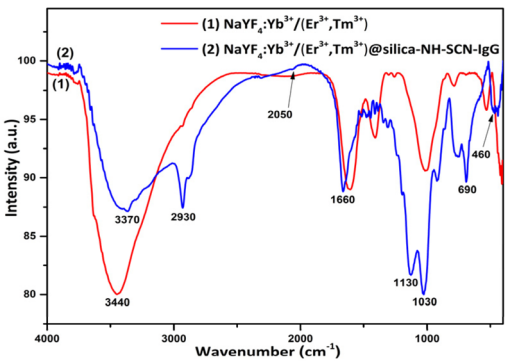

Fig. 4 FTIR spectra of $NaYF_4$:Yb^{3+}/(Er^{3+},Tm^{3+}) nanoparticles before (1) and after (2) surface functionalization with silica–NH–SCN–IgG.

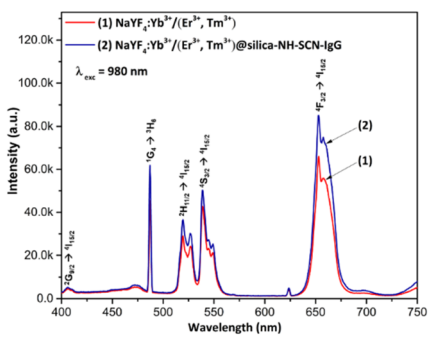

Fig. 5 UCPL spectra of $NaYF_4$:Yb^{3+}/(Er^{3+},Tm^{3+}) (1) and $NaYF_4$:Yb^{3+}/(Er^{3+},Tm^{3+})@silica–NH–SCN–IgG nanoparticles (2) under 980 nm excitation.

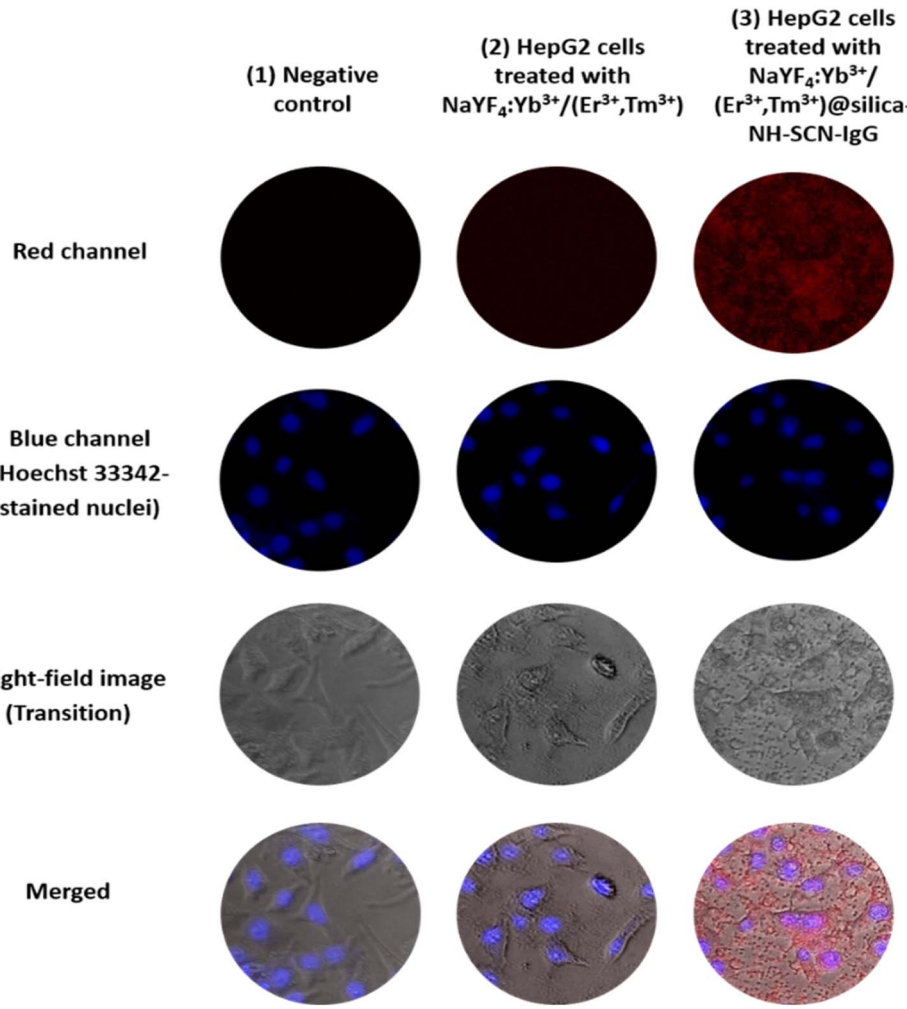

Fig. 6 Fluorescence microscopy images of HepG2 cells treated with (1) negative control (no nanoparticles), (2) $NaYF_4$:Yb^{3+}/(Er^{3+},Tm^{3+}) and (3) $NaYF_4$:Yb^{3+}/(Er^{3+},Tm^{3+})@silica–NH–SCN–IgG.

attributed to overlapping ($^2H_{11/2}$, $^4S_{3/2}$) → $^4I_{15/2}$ transitions of Er^{3+}, respectively. These results confirm efficient energy transfer from Yb^{3+} sensitizers to both Er^{3+} and Tm^{3+} activators within the $NaYF_4$ host matrix.

Notably, the surface-modified nanoparticles $NaYF_4$:Yb^{3+}/(Er^{3+},Tm^{3+})@silica–NH–SCN–IgG (curve 2) exhibits enhanced emission intensity compared to the uncoated core (curve 1). This enhancement may be attributed to the silica shell's ability to reduce surface-related quenching, protect the luminescent core, and potentially improve light scattering or local field effects. The preservation and even enhancement of dual-color emission (blue and red) after surface modification confirms that the core crystal quality is maintained and the functional coating is compatible with upconversion luminescence. Among the three emission bands, the red emission (~660 nm) is dominant. This result supports the material's suitability for fluorescence imaging in biological labeling applications.

3.4. *In vitro* cellular labeling

To evaluate the bio-recognition performance of the synthesized nanomaterials, fluorescence labeling experiments were applied in HepG2 liver cancer cells. Fig. 6 presents the comparative fluorescence microscopy images of: (1) negative control, (2)

Table 1 Percentage of fluorescent HepG2 cells determined by flow cytometry

Samples	Fluorescent cell population (%)
Negative control (no nanoparticles)	3.68
HepG2 – $NaYF_4$:Yb^{3+}/(Er^{3+},Tm^{3+})	3.13
HepG2 – NaYF: Yb^{3+}/(Er^{3+},Tm^{3+})@silica–NH–SCN–IgG	18.10

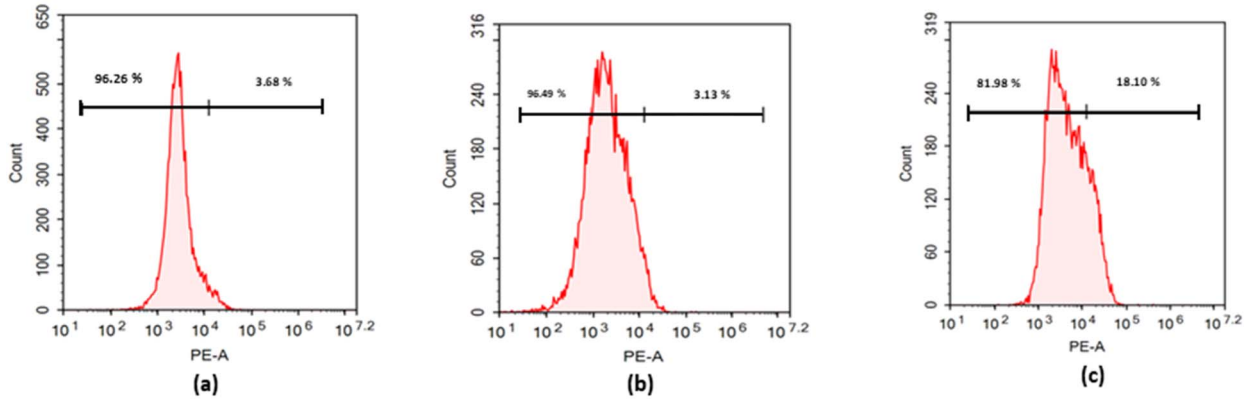

Fig. 7 Flow cytometry analysis of HepG2 cells labelled with: (a) negative control (no treatment), (b) $NaYF_4:Yb^{3+}/(Er^{3+},Tm^{3+})$ and (c) $NaYF_4:Yb^{3+}/(Er^{3+},Tm^{3+})$@silica–NH–SCN–IgG.

HepG2 cells treated with $NaYF_4:Yb^{3+}/(Er^{3+},Tm^{3+})$, and (3) HepG2 cells treated with $NaYF_4:Yb^{3+}/(Er^{3+},Tm^{3+})$@silica–NH–SCN–IgG. For each condition, red channel (upconversion luminescence), blue channel (Hoechst 33 342 nuclear stain), bright-field (transition) and merged images are provided.

In the negative control group, no red fluorescence was observed, as expected. Cells treated with unmodified UCNPs $NaYF_4:Yb^{3+}/(Er^{3+},Tm^{3+})$ showed weak and diffuse red signals, likely resulting from nonspecific adsorption or limited uptake. In stark contrast, HepG2 cells treated with SCN–IgG-functionalized nanoparticles $NaYF_4:Yb^{3+}/(Er^{3+},Tm^{3+})$@silica–NH–SCN–IgG exhibited intense and localized red fluorescence co-localized with the nuclei, demonstrating effective and selective cellular targeting.

The enhanced targeting is attributed to the role of thiocyanate (–SCN) groups, which form stable thiourea bonds with the primary amine groups of IgG antibodies. This covalent conjugation preserves the bioactivity of IgG, allowing it to serve as a molecular recognition element that specifically binds to surface antigens on HepG2 cells. Notably, no significant red signal was detected in the normal control cells (HEK-293A, data not shown), supporting the selective targeting capability of the SCN–IgG system.

The merged fluorescence images further highlight this selectivity, with clear co-localization of red (UCNP) and blue (nucleus) signals, confirming successful surface binding without off-target fluorescence. These results demonstrate that the developed nanoprobes effectively combine bright upconversion luminescence with ligand-directed specificity for potential use in targeted liver cancer diagnostics.

3.5. Cellular uptake analysis using flow cytometry

To evaluate the cellular penetration ability of the synthesized upconversion nanoprobes, flow cytometry analysis was conducted on HepG2 liver cancer cells incubated with different nanoparticle formulations. The fluorescence signal (PE-A channel) was quantitatively analyzed to determine the percentage of fluorescent cell population as shown in Table 1 and illustrated in Fig. 7.

Table 1 shows that both the negative control (untreated cells) and the group treated with non-functionalized $NaYF_4:Yb^{3+}/(Er^{3+},Tm^{3+})$ nanoparticles exhibited minimal fluorescence, with positive populations of only 3.68 and 3.13%, respectively. This indicates negligible non-specific cellular uptake. In contrast, HepG2 cells treated with the IgG-conjugated nanoprobes ($NaYF_4:Yb^{3+}/(Er^{3+},Tm^{3+})$@$SiO_2$–NH–SCN–IgG) displayed a markedly higher fluorescent cell population of 18.10%, clearly indicating enhanced cellular binding and uptake due to IgG-mediated recognition. These findings are further corroborated by the flow cytometry histograms in Fig. 7, which demonstrate a significant shift in fluorescence intensity in the IgG-conjugated group compared to the other two. The enhanced signal confirms the successful targeting ability of the functionalized nanoprobes.

Thus, the results of cellular uptake analysis provide compelling evidence that the surface modification—particularly IgG conjugation – significantly improves the targeting and cellular uptake of the upconversion nanoparticles. This reinforces their potential applicability in selective liver cancer cell imaging.

4. Conclusions

In this study, $NaYF_4:Yb^{3+}/(Er^{3+},Tm^{3+})$ upconversion nanoparticles were successfully synthesized and sequentially functionalized with silica, thiocyanate, and IgG to enhance their biocompatibility and targeting capability. The resulting nanoprobes exhibited high crystallinity, uniform nanoscale morphology, and strong upconversion luminescence under 980 nm excitation, with dominant red emission.

Surface modification with silica and SCN–IgG preserved or enhanced luminescence intensity while enabling selective cellular recognition. Fluorescence microscopy and flow cytometry confirmed specific labeling of HepG2 liver cancer cells, achieving a labeling efficiency of 18.10% in the IgG-conjugated group – significantly higher than in control samples.

These results demonstrate the potential of SCN–IgG-functionalized $NaYF_4:Yb^{3+}/(Er^{3+},Tm^{3+})$ nanoparticles as highly

selective and luminescent nanoprobes for targeted fluorescence imaging in liver cancer diagnostics.

Data availability

All data supporting the findings of this study, including figures and tables, are available within the article. Additional datasets are available from the corresponding author upon reasonable request.

Author contributions

Ha Thi Phuong: methodology, investigation, formal analysis, data curation, conceptualization. Le Thi Vinh: writing – original draft, methodology, investigation, formal analysis. Do Thi Thao: methodology, investigation, formal analysis. Le Anh Tu: methodology, formal analysis. Tong Quang Cong: methodology, investigation. Nguyen Duc Van: writing – review & editing. Tran Quoc Tien: methodology, formal analysis, writing – review and editing. Tran Thu Huong: writing – review & editing, methodology, investigation, formal analysis, conceptualization and editing the final manuscript. All the authors have read and agreed to the published version of the manuscript.

Conflicts of interest

The authors declare that there is no conflicts of interest regarding the publication of this paper.

Acknowledgements

This research is funded by the Vietnam Academy of Science and Technology under Grant No. VAST03.03/23-24.

References

1 J. Zhou, Z. Liu and F. Li, Upconversion Nanophosphors for Small-Animal Imaging, *Chem. Soc. Rev.*, 2012, **41**, 1323–1349.
2 Y. Liu, D. Tu, H. Zhu, E. Ma and X. Chen, Lanthanide-doped luminescent nano-bioprobes: from fundamentals to biodetection, *Nanoscale*, 2013, **5**, 1369–1384.
3 G. Chen, H. Qiu, P. N. Prasad and X. Chen, Upconversion Nanoparticles: Design, Nanochemistry, and Applications in Theranostics, *Chem. Rev.*, 2014, **114**(10), 5161–5214.
4 M. Wang, G. Abbineni, A. Clevenger, C. Mao and S. Xu, Upconversion Nanoparticles: Synthesis, Surface Modification and Biological Applications, *Nanomed. Nanotechnol. Biol. Med.*, 2011, **7**(6), 710–729.
5 K. Chen, Q. Luan, T. Liu, B. Albinsson and L. Hou, Semiconductor nanocrystals-based triplet-triplet annihilation photon-upconversion: Mechanism, materials and applications, *Responsive Mater.*, 2025, **3**(1), e20240030.
6 A. A. Doronkina, V. I. Kochubey, A. V. Maksutova, *et al.*, $NaYF_4$:Yb,Er Upconversion Nanoparticles for Imaging: Effect on Red Blood Cells, *Photonics*, 2023, **10**, 1386.
7 Y. Yaoguang, C. Gang, Z. Yansong and H. Zhonghui, Recent advances in rare-earth elements modification of inorganic semiconductor-based photocatalysts for efficient solar energy conversion, *J. Rare Earths*, 2015, **33**(5), 453–462.
8 F. Kang, J. He, T. Sun, Z. Y. Bao, F. Wang and D. Y. Lei, Plasmonic Dual-Enhancement and Precise Color Tuning of Gold Nanorod@SiO2 Coupled Core–Shell–Shell Upconversion Nanocrystals, *Adv. Funct. Mater.*, 2017, **27**(36), 1701842.
9 F. Wang and X. Liu, Upconversion Multicolor Fine-Tuning: Visible to Near-Infrared Emission from Lanthanide-Doped $NaYF_4$ Nanoparticles, *J. Am. Chem. Soc.*, 2008, **130**, 5642–5643.
10 F. Wang and X. Liu, Recent Advances in the Chemistry of Lanthanide-Doped Upconversion Nanocrystals, *Chem. Soc. Rev.*, 2009, **38**, 976–989.
11 J. Zhou, Q. Liu, W. Feng, Y. Sun and F. Li, Upconversion Luminescent Materials: Advances and Applications, *Chem. Rev.*, 2015, **115**(1), 395–465.
12 B. Zhou, B. Shi, D. Jin and X. Liu, Controlling Upconversion Nanocrystals for Emerging Applications, *Nat. Nanotechnol.*, 2015, **10**, 924–936.
13 M. Haase and H. Schäfer, Upconverting Nanoparticles, *Angew. Chem., Int. Ed.*, 2011, **50**(26), 5808–5829.
14 L. Gaofeng, W. Haojie, S. Hao, W. Haitao, Z. Mengxi, J. Aihua, L. Jinghua and L. Guangda, Recent progress in the development of upconversion nanomaterials in bioimaging and disease treatment, *J. Nanobiotechnol.*, 2020, **18**, 154.
15 T. T. Huong, H. T. Phuong, L. T. Vinh, H. T. Khuyen, D. T. Thao, L. D. Tuyen, T. K. Anh and L. Q. Minh, Upconversion $NaYF_4$:Yb^{3+}/Er^{3+}@silica-TPGS bio-nano complexes: synthesis, characterization, and *in vitro* test for labelling cancer cells, *J. Phys. Chem. B*, 2021, **125**, 9768–9775.
16 H. T. Phuong, L. T. Vinh, T. Q. Cong, T. Q. Tien, N. D. Van, V. T. H. Ha, V. N. Phan, L. T. Hoi, P. D. Thang, D. T. Thao and T. T. Huong, Optimized $NaYF_4$: Er^{3+}/Yb^{3+} Upconversion Nanocomplexes *via* Oleic Acid for Biomedical Applications, *Inorganics*, 2025, **13**, 1–22.
17 S. Wen, J. Zhou, K. Zheng, A. Bednarkiewicz, X. Liu and D. Jin, Advances in highly doped upconversion nanoparticles, *Nat. Commun.*, 2018, **9**, 2415.
18 F. Zhang, Y. Wan, T. Yu, F. Zhang, Y. Shi, S. Xie, Y. Li, L. Xu, B. Tu and D. Zhao, Uniform Nanostructured Arrays of Sodium Rare-Earth Fluorides for Highly Efficient Multicolor Upconversion Luminescence, *Angew. Chem., Int. Ed.*, 2007, **46**(42), 7976–7979.
19 D. Gao, G. Dangli, Z. Xiangyu, Z. Hairong, S. Peng, L. Long and L. Yawen, Codopant ion-induced tunable upconversion emission in β-$NaYF_4$:Yb^{3+}/Tm^{3+} nanorods, *Dalton Trans.*, 2013, **42**, 1834–1841.
20 C. Hongjin, X. Juan, Z. Baozhou, L. Botong, X. Shuilin, R. Na, X. Xiaoji, H. Ling and H. Wei, Rare Earth Ion-Doped Upconversion Nanocrystals: Synthesis and Surface Modification, *Nanomaterials*, 2015, **5**, 1–25.
21 A. J. Rufaihah and Z. Yong, Biocompatibility of silica coated $NaYF_4$ upconversion fluorescent nanocrystals, *Biomaterials*, 2008, **29**(30), 4122–4128.

22 H. Dong, L.-D. Sun and C.-H. Yan, Energy Transfer in Lanthanide Upconversion Studies for Extended Optical Applications, *Chem. Soc. Rev.*, 2015, **44**, 1608–1634.
23 M. K. Gnanasammandhan, N. M. Idris, A. Bansal, K. Huang and Y. Zhang, Near-infrared photoactivation using mesoporous silica–coated $NaYF_4$:Yb,Er/Tm upconversion nanoparticles, *Nat. Protoc.*, 2016, **11**, 688–713.
24 X. Tang, Y. Han, W. Zhou, W. Shen and Y. Wang, A FRET Based Composite Sensing Material Based on UCNPs and Rhodamine Derivative for Highly Sensitive and Selective Detection of Fe^{3+}, *J. Fluoresc.*, 2023, **33**(6), 2219–2228.
25 Z. Li, Y. Zhang and S. Jiang, Multicolor Core/Shell-Structured Upconversion Fluorescent Nanoparticles, *Adv. Mater.*, 2008, **20**(24), 4765–4769.
26 H. Chu, T. Cao, G. Dai, B. Liu, H. Duan, C. Kong, N. Tian, D. Hou and Z. Sun, Recent Advances in Functionalized Upconversion Nanoparticles for Light-Activated Tumor Therapy, *RSC Adv.*, 2021, **11**, 35472–35488.
27 C. P. Alonso, *et al.*, Synthesis, characterization and application in HeLa cells of NIR light responsive doxorubicin delivery system based on $NaYF_4$:Yb,Tm@SiO_2-PEG nanoparticles, *ACS Appl. Mater. Interfaces*, 2015, **7**(27), 14992–14999.
28 C. Yueying, W. Jiehua, Z. Xianlin, L. Yanling, A. P. James, L. Yiqing and H. P. Nicolle, Assessing the activity of antibodies conjugated to upconversion nanoparticles for immunolabeling, *Anal. Chim. Acta*, 2022, **1209**, 339863.
29 C. Wang, L. Cheng and Z. Liu, Upconversion nanoparticles for photodynamic therapy and other cancer therapeutics, *Theranostics*, 2013, **3**(5), 317–330.
30 R. Wei, W. Shihui, A. T. Sherif, P. S. Qian, L. Gungun, A. J. Lining, J. F. Michael, G. Harshad, M. O. Antoine and J. Dayong, Anisotropic functionalization of upconversion nanoparticles, *Chem. Sci.*, 2018, **9**(18), 4352–4358.
31 H. Chu, L. Wang, Y. Zhu, X. Yu and Y. Wang, Recent advances in functionalized upconversion nanoparticles for light-activated tumor therapy, *RSC Adv.*, 2021, **11**(56), 35472–35488.
32 M. B. Audet, B. Byrne and S. G. Kazarian, High-Throughput Thermal Stability Analysis of a Monoclonal Antibody by Attenuated Total Reflection FT-IR Spectroscopic Imaging, *Anal. Chem.*, 2014, **86**, 9786–9793, DOI: **10.1021/ac502529q**.
33 A. Sadat and I. J. Joye, Peak Fitting Applied to Fourier Transform Infrared and Raman Spectroscopic Analysis of Proteins, *Appl. Sci.*, 2020, **10**(5918), 1–16, DOI: **10.3390/app10175918**.
34 S. Niekamp, N. Stuurman and R. D. Vale, A 6-nm ultra-photostable DNA FluoroCube for fluorescence imaging, *Nat. Methods*, 2020, **17**, 437–441.
35 R. G. Geitenbeek, P. T. Prins, W. Albrecht, A. V. Blaaderen, B. M. Weckhuysen and A. Meijerink, $NaYF_4$:Er^{3+},Yb^{3+}/SiO_2 Core/Shell Upconverting Nanocrystals for Luminescence Thermometry up to 900 K, *J. Phys. Chem. C*, 2017, **121**, 3503–3510.
36 T. M. Stauffer, *Applications of Molecular Spectroscopy to Current Research in the Chemical and Biological Sciences - Fourier Transform Infrared and Raman Characterization of Silica-Based Materials*, Larissa Brentano Capeletti and João Henrique Zimnoch, Intech, 2016, ch. 1, pp. 1–20.